frontiers
in Earth Science

TYPE Original Research
PUBLISHED 13 March 2026
DOI 10.3389/feart.2026.1738377

EDITED BY
Paolo Capuano,
University of Salerno, Italy

REVIEWED BY
Grazia De Landro,
University of Naples Federico II, Italy
Monika Staszek,
Polish Academy of Sciences, Poland

*CORRESPONDENCE
Emmanuel Gaucher,
✉ emmanuel.gaucher@kit.edu

RECEIVED 03 November 2025
REVISED 04 February 2026
ACCEPTED 05 February 2026
PUBLISHED 13 March 2026

CITATION
Gaucher E, Lengliné O and Schmittbuhl J (2026) Seismic interplay during the GRT-1 stimulation series of the Rittershoffen EGS reservoir. *Front. Earth Sci.* 14:1738377. doi: 10.3389/feart.2026.1738377

# Seismic interplay during the GRT-1 stimulation series of the Rittershoffen EGS reservoir

Emmanuel Gaucher[1]*, Olivier Lengliné[2] and Jean Schmittbuhl[2]

[1]Geothermal Energy and Reservoir Technology, Institute of Applied Geosciences, Karlsruhe Institute of Technology, Karlsruhe, Germany, [2]EOST/ITES, University of Strasbourg/CNRS, UMR7063, Strasbourg, France

Between April and June 2013, the GRT-1 well, located at the Rittershoffen EGS geothermal site in the Upper Rhine Valley (France), underwent three distinct stimulations: a thermal stimulation, a chemical stimulation, and finally a hydraulic stimulation. These stimulations, in particular the hydraulic stimulation, have been previously explored by several studies. The current study addresses a feature that has been less analyzed: the possible seismic interplay between these stimulations. By applying improved template matching and a relative location method, a comprehensive catalog of more than 3000 seismic events was established, covering the three stimulations. This catalog allows tracking and comparison of reservoir seismogenic responses to successive, yet different, stimulation types with high spatial and temporal precision. We present the evolution of several indicators such as event distribution and clustering, b-value, and seismic injection efficiency across the stimulations. The observed differences raise the question of the relevance of using previous stimulation indicators to anticipate seismogenic behavior during subsequent stimulations. We also evidence simultaneous seismicity migration, decrease of the instantaneous injection index and decrease of the seismic efficiency at the end of the hydraulic stimulation but prior to the most energetic burst of seismicity that occurred 4.5 days after shut-in.

KEYWORDS
**enhanced geothermal system (EGS), induced seismicity, seismic efficiency, stimulation, Upper Rhine Graben**

## 1 Introduction

Large fault zones are important targets for the development of deep geothermal reservoirs because adjacent damage zones and/or highly fractured zones are likely to be more permeable than surrounding formations if not sealed by secondary mineralizations and offer zones of facilitated circulation of geothermal fluids (Vidal and Genter, 2018). However, if the permeability of the fault zone is insufficient to enable economic geothermal exploitation, the connection between the well and the reservoir must be improved by stimulation, leading to a so-called enhanced geothermal system (EGS). Therefore, this EGS technology has the potential to make geothermal energy production and direct-use heating accessible in any region of the world, independently of conventional geothermal resources (IEA, 2024). Fault zones, however, are also zones that have experienced seismic episodes in the past and that may still present a non-negligible seismic hazard.

The stimulations rely on the injection of fluids from the well into the formation, however, the processes expected to improve fluid flow may vary. Thus, in addition to hydraulic stimulation, which is the most commonly used for the development of EGS to date (Breede et al., 2013), thermal or chemical stimulations can also be applied (Li et al., 2022). Chemical stimulation should dissolve minerals that seal fluid pathways and change their mechanical properties through alteration (Portier et al., 2009). Thermal and hydraulic stimulations are based on geomechanical processes that lead to fracturing, i.e., the generation of new surfaces in the formation, or shearing of existing fractures and faults, according to the pre-existing state of stresses in the reservoir (Axelsson et al., 2006; Cornet et al., 2007; Jeanne et al., 2014; Norbeck et al., 2018). In the former approach, the creation of high thermal stresses in the formation is expected, while, in the latter, a high pore-pressure increase is foreseen as the main driver of the rupture in order to reduce effective normal stresses. In thermal stimulation, the fluid is injected generally at flow rates lower than those in hydraulic stimulation but for a longer period, whereas in hydraulic stimulation the goal is to reach the nominal economical flow rate step by step. In all cases, the injected fluid is forced to circulate by the surface pumps.

However, the real effects of the stimulation(s) away from the well are difficult to ascertain, as they occur beyond the scope of observation tools of well logging. One way to gain insight into these effects is by analyzing the seismicity induced by mechanical instabilities initiated during stimulation (Majer et al., 2007; Evans et al., 2012; Zang et al., 2014). In fact, valuable information regarding the geomechanical behavior and geometry of the fault system in reaction to stimulation(s) can be derived from the seismic activity, which results from rock failure and fault/fracture slip in areas necessarily affected by stress changes caused by fluid injection. Paradoxically, this can also help to identify aseismic slips (Schmittbuhl et al., 2014). Seismicity is also crucial for the assessment and forecasting of induced seismic risks (Gaucher et al., 2015). In fact, induced or triggered earthquakes could directly affect the population when they become large (typically greater than magnitude 2 to be felt and magnitude 3.5 to induce building damage). In this case, they should be prevented or mitigated (Grigoli et al., 2017) otherwise stimulation could ultimately lead to abandonment of the geothermal site (Häring et al., 2008; Ellsworth et al., 2019; Schmittbuhl et al., 2021), which would constitute a failure for all stakeholders.

Many studies analyze specific stimulation operations from the associated seismicity (e.g., Baisch et al., 2006; Cuenot et al., 2008; Kraft and Deichmann, 2014; Kwiatek et al., 2015; Hofmann et al., 2021; McLennan et al., 2023). However, it is much less common to analyze series of stimulations carried out in the same well, after drilling, in a reservoir initially devoid of any seismicity. Only recently, Drif et al. (2024) did such an analysis for the Soultz-sous-Forêts (France) geothermal site. In fact, attention often focuses on hydraulic stimulation, which is the most prone to generate seismicity. In addition, despite improvements in local seismicity data processing, the interpretation of the results with regard to the stimulation operations remains very limited due to missing public information on the history of fluid injection.

In this study, we focus on the seismicity induced by the series of stimulations carried out, in the GRT-1 well, at the Rittershoffen enhanced geothermal site (Alsace, France) (Figure 1). This site is located in the Upper Rhine Valley, an area prone to deep geothermal exploitation and development, as underlined by the number of active or planned sites in France and Germany (Maurer et al., 2020). Actually, Rittershoffen is less than 10 km from Soultz-sous-Forêts. The GRT-1 and GRT-2 wells of the plant were drilled to a depth of 2.5 km (Baujard et al., 2017). The open-hole section of each well crosses the transition zone between the sedimentary cover of Triassic sandstone and the Paleozoic granitic basement, and intersects a major fault system characterized by an apparent normal offset of about 220 m. Unlike GRT-2, the geothermal resource could not be exploited from GRT-1 given the poor initial hydraulic conditions. Therefore, a sequence of thermal, chemical, and hydraulic stimulations was carried out in this well, between April and June 2013 (Baujard et al., 2017). Individual injections were conducted along the same depth interval and have been continuously monitored by at least 12 surface seismic stations within a 15-km distance from the wellhead (Maurer et al., 2015; Lengliné et al., 2017; Maurer et al., 2020). These operations did not generate felt seismicity and multiplied the injectivity index of the well by a factor of five (Baujard et al., 2017). Since May 2016, the plant has been continuously operating and provides heat from a 170 °C geothermal fluid produced on the surface at up to 250 $m^3$/h (Lengliné et al., 2025).

The current study extends the results of Lengliné et al. (2017) where only the hydraulic stimulation of GRT-1 and the associated post-stimulation seismicity were considered, disregarding previous stimulations. It also complements the work of Maurer et al. (2020) where the authors were limited in their interpretation of the results due to questionable absolute locations of seismicity, especially depth, and because neither template matching nor relative locations were applied. Following the data processing workflow of the present study, we have been able to compile a complete and reliable seismicity catalog that covers the three phases of GRT-1 stimulation. This catalog is first described and then analyzed in light of the stimulations considered either independently or in series. Hence, we discuss the evolution of several characteristics, such as spatial distribution and clustering of events, b-value, seismic injection efficiency, and raise the question of the relevance of using previous stimulations to better understand the response of the reservoir and anticipate its behavior in the face of subsequent stimulations.

## 2 Data and methods

### 2.1 Seismological data

The Rittershoffen geothermal site has been continuously monitored by several local seismic networks since the start of drilling operations in 2012 (Gaucher et al., 2019; Maurer et al., 2020). During all stages of reservoir development, a permanent network made up of 12 surface stations was active: four stations were dedicated to the Rittershoffen field, while the other eight focused on the nearby Soultz-sous-Forêts geothermal site. During the thermal stimulation of GRT-1, the permanent network was the only one operating; however, in June 2013, five temporary stations were added to monitor the chemical and hydraulic stimulations of GRT-1. On 3<sup>rd</sup> of July, three temporary supplementary stations were installed. Figure 1 shows the distribution of all seismic stations that monitor GRT-1 stimulations. Details about these stations can be found in Maurer et al. (2020).

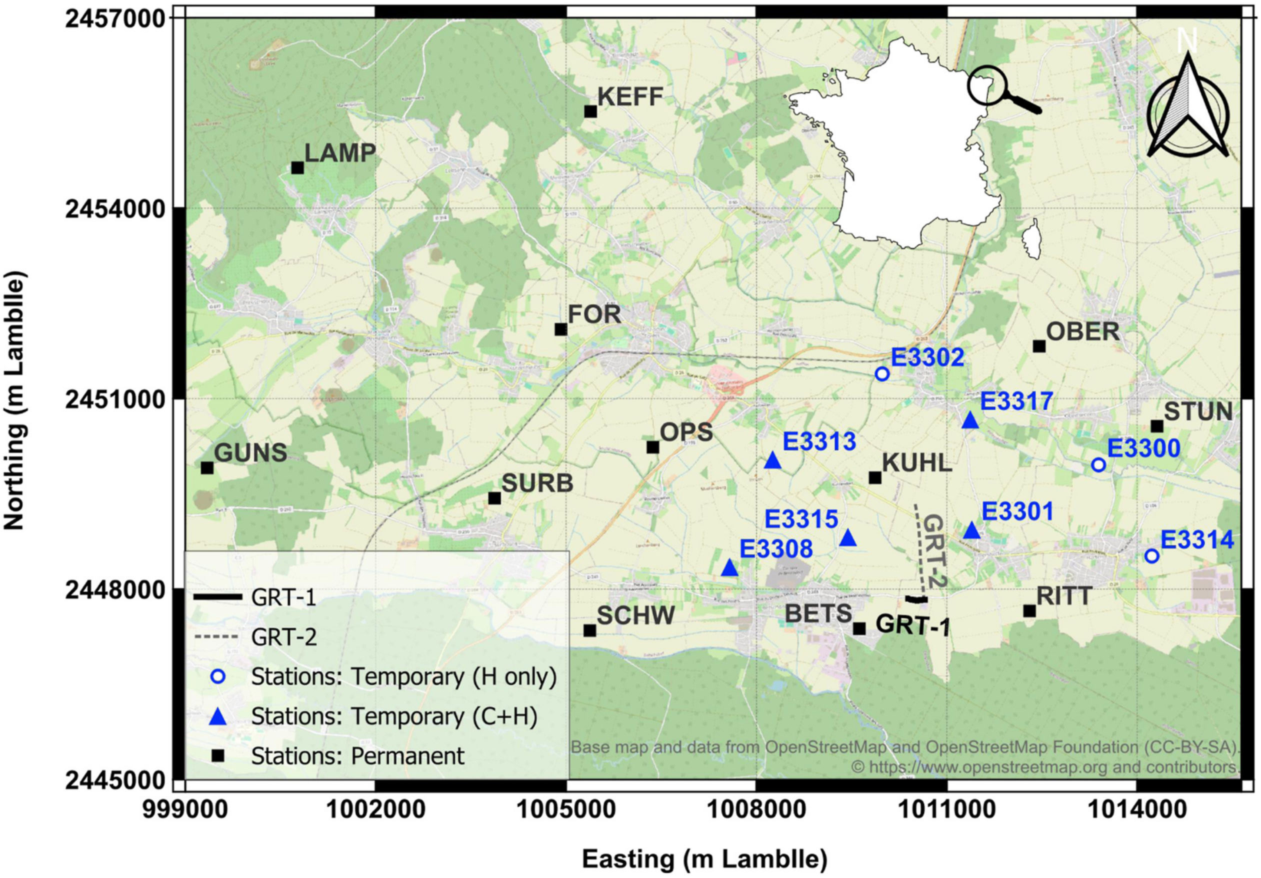

FIGURE 1
Overview map of the position of the seismic monitoring stations and of the Rittershoffen well trajectories GRT-1 and GRT-2. The small insert shows the study area on the map of France. Metric coordinates are in Lambert II extended (EPSG 27572).

The thermal stimulation of GRT-1 took place from 23 to 26 April 2013 (Baujard et al., 2017). Following a pre-stimulation injection test on 22 June 2013, the three phases of chemical stimulation were carried out between 23 and 26 June 2013. Finally, hydraulic stimulation occurred on 27 and 28 June 2013. It should be noted that during the so-called thermal and hydraulic stimulations, the temperature of the injected fluid was close to 10 °C in both cases Maurer et al. (2020). Consequently, the main operational differences between the two stimulations lay in the injection rates and durations applied. During stimulations, injection flow rates and wellhead pressures were measured (Baujard et al., 2017); however, wellhead pressures for chemical stimulation are not reliable (V. Maurer, personal communication).

The continuous seismological dataset under study covers the period from 24/04/2013 00:00:00 to 05/07/2013 00:00:00 (UTC).

## 2.2 Data processing

### 2.2.1 Template matching

To generate a high resolution seismological catalog, template matching was applied on continuous data using all events in the catalog provided by Maurer et al. (2020) as templates. These events were detected using a calibrated "short-term average over long-term average" (STA/LTA) method and reviewed by an operator in a systematic way. Therefore, the original catalog does not contain false events, has accurate and checked wave-arrival picks, and probably gathers the typical signatures of the seismicity induced at Rittershoffen by the stimulations. However, six of these events were discarded from the templates because they were too far away from the GRT-1 injection.

The template matching algorithm applied follows Lengliné et al. (2017) and Lengliné (2022) with an automatic selection of the correlation detection threshold according to Slinkard et al. (2014) and Slinkard et al. (2016). The template window for detection is 2.56 s long and starts 0.5 s before the P-wave arrival. It is long enough to include the S-wave arrival since the maximum delay observed at one station between both wave arrivals is 1.9 s. Before correlation, all waveforms are resampled to 100 Hz and filtered between 10 and 45 Hz (Butterworth filter of order 4). These values were chosen after comparative analysis of the power spectral density of the template waveforms with periods of noise, for each channel. We built a list of all seismic stations ranked according to the number of available P and S wave picks in the template catalog. Then, correlation is computed on the first six channels of this list for which template and continuous waveforms are available. Since the seismic network expanded between the thermal, chemical and hydraulic stimulations, the channel list varies accordingly. However, among the stations and channels most often used for detection (i.e., that are most frequently picked), three are permanent stations that were monitoring all stimulation phases. The template matching returns the average Pearson correlation coefficient at each time step measured over the six channels, which has to exceed a given threshold for a new event to be extracted. This detection threshold is calculated automatically for each day and for each template, in order to guaranty a daily false detection rate smaller than 1/10,000. It is obtained by running template matching over 1 day of data with the time- and polarity-reversed versions of the template waveforms, which should not detect new events but does account for the template signal features (i.e., signal-to-noise ratio, time-frequency content) and the network layout (i.e., interstation distance, geometry). This processing flow was proposed by Slinkard et al. (2014) and Slinkard et al. (2016) and resulted in a median value of the detection thresholds equal to 0.41. More details about the statistical distribution of the thresholds can be found in the Supplementary Figure S1.

Several template events have similar waveforms, which led to multiple detections of the same new event. To remove duplicates in the final catalog, the event detection times were compared, and if they were separated by less than one second, the detections were merged and assigned to the template that detected the event with the highest correlation.

### 2.2.2 Relative location

After template matching, all new and original events were first located using the NonLinLoc software (Lomax et al., 2000; 2009; Lomax, 2023) in a 3-D velocity model of the area, which is publicly available (Lengliné et al., 2023). This provides the initial absolute locations of the events before their relative location.

The high waveform similarities of the events detected by the same template enable us to determine with high precision the associated P- and S-wave arrival times using focused cross-correlation. Hence, for all possible event pairs, similar channels are cross-correlated over a 1.1 s window centered on the seismic wave arrivals. The vertical channels are considered for the P-wave arrivals and the horizontal ones for the S-wave arrivals. The template events have well-determined P- and S-wave arrivals. However, for the newly detected events, initial P-wave arrivals were set according to the P-wave travel time of the corresponding template and relative to the time of maximum correlation during the detection step. To determine the initial arrival time of the S wave, the travel time of the P wave of the template and a P- to S-wave velocity ratio of 1.9 were used. Then, the obtained arrival time differences are considered for relative location only if the correlation coefficient was higher than or equal to 0.5 and if, for the same event pair, this threshold applies for six channels at least. This screening ensures that the relation of an event pair is stable and prevents outliers from being given too much weight during location inversion.

The relative location is performed with Growclust3D software (Trugman et al., 2022; Trugman, 2023a; Trugman, 2023b), using the same 3-D velocity model. We follow the approach of Ross et al. (2019) and give a 10-times larger weight to travel times delays computed for a pair of template events than for the other pairs in order to increase the stability of the resolved location. For cross-correlated events, 30 bootstrap iterations were applied to quantify the relative precision of the hypocenters (defined as the uncertainty in the following). The rest of the parameters follow the default values taken in the GrowClust3D software. Finally, all hypocenters were shifted to position the first event of the thermal stimulation at 2352 m true vertical depth in GRT-1, where a major fracture has been observed (Vidal et al., 2017), exactly at 1010421.7 m Easting, 2447837.2 m Northing[1]) and 2201 m below sea level (b.s.l.). This fracture, which is more than 20 cm thick, is considered as a major drain that controls the well hydraulics (Vidal et al., 2016; Baujard et al., 2017). The same reference point was used by Lengliné et al. (2025), whose relative locations are consistent with those of Lengliné et al. (2017) where all events were initially located on the borehole trajectory at 2300 m depth. Hence, the results reported in the two previous references can be compared to ours directly or can complement them. Although there is no independent measurement of the absolute distance from the well for this first event, seismicity induced by injection generally initiates or is considered to initiate in the vicinity of the well (e.g., Goebel and Brodsky, 2018; Danré et al., 2024). Thus, the assumption of taking this point at the well level as a reference can be considered reasonable.

### 2.2.3 Magnitudes

For the new events, the magnitudes are calculated from the local magnitude, $M_{Lv}$, of the corresponding template event found in the catalog of Maurer et al. (2020). At first, the magnitude of each template was corrected from the newly obtained hypocenter, then the ratio of the maximum waveform amplitudes between the template and the new event was used to estimate the magnitude difference. In addition, a conversion from $M_{Lv}$ to moment magnitude $M_W$ was done. This was a two-step conversion, first from $M_{Lv}$ to $M_{Lh}$ and then from $M_{Lh}$ to $M_W$ as proposed by Bagagli et al. (2022) and Bethmann et al. (2011), respectively. Hence, $M_W = 0.9097 + 0.5754\ M_{Lv}$.

# 3 Results

## 3.1 Event catalog statistics

The seismological catalog obtained by applying the processing workflow described in Section 2 contains 3298 seismic events. This almost triples the number of events in the catalog provided by Maurer et al. (2020), which underlines the relevance of completing the catalog using template matching. Table 1 details the number of seismic events detected and located (column "Final"), and the number of events relatively located (column "Reloc"), for each operational phase of GRT-1 development (defined by Baujard et al. (2017)) and for the post-hydraulic seismic sequence.

---

[1] The metric coordinate system called Lambert II extended (EPSG 27572) is the default system used unless specified.

TABLE 1 **Seismic event statistics per operational phase conducted in GRT-1.**

| Operational phases | Templates | Final | Reloc | $Q_{MAX}$ (l/s) | $WHP_{MAX}$ (MPa) | Volume ($m^3$) | Duration (h) | $I_{Index}$ (l/s/bar) |
|---|---|---|---|---|---|---|---|---|
| Thermal stimulation 23/04–26/04 | 146 | 328 | 291 | 25 | 2.8 | 4230 | 62.6 | 0.9 |
| Injection test 22/06–23/06 12:00 | 0 | 3 | 0 | 27 | 2.5 | 357 | 6.5 | - |
| Chemical stimulation 23/06 12:00–27/06 | 0 | 2 | 2 | 5 | n.a | 269 | 14.2 | 1.7 |
| Hydraulic stimulation 27/06–28/06 16:00 | 822 | 2468 | 2461 | 80 | 3.3 | 4000 | 28.2 | 2.5 |
| Post-hydraulic 28/06 16:00–04/07 | 162 | 497 | 487 | 0 | 0 | 0 | 0 | - |
| Total | 1130 | 3298 | 3241 | - | - | 8856 | - | - |

In parallel are presented: the number of events of the initial reference catalog (column "Templates"), the final number of events of our catalog (column "Final"), the number of relative located events (column "Reloc"), as well as several parameters of the stimulation operations: maximum flow rate $Q_{MAX}$(in l/s), maximum wellhead pressure $WHP_{MAX}$(in MPa), total volume injected (in $m^3$), injection duration (in hours) and injectivity index $I_{Index}$(in l/s/bar). These parameters are extracted from Baujard et al. (2017) and Maurer et al. (2020). The year is 2013.

The template matching more than tripled the number of events associated with hydraulic stimulation and the post-hydraulic phase compared to the initial catalog and doubled it compared to the results obtained by Lengliné et al. (2017). The procedure also more than doubled the number of events associated with thermal stimulation. Five events have been detected between 22 June and 26 June, i.e., the period containing injection test and chemical stimulation, while none was initially present in the Maurer et al. (2020) catalog (no templates are available for this period). The three events that occurred after the injection test but before chemical stimulation were not relatively located because they were not correlated with any other event and their magnitudes are smaller than −0.82 $M_{Lv}$. The two events detected during the period of chemical stimulation present very large hypocenter uncertainties, more than 260 m horizontally and 184 m vertically, as well as large origin time uncertainties, more than 20 ms. So, the locations are not of good quality (see Section 3.3 for more details). Furthermore, an inspection of the traces of these five events at several stations suggests that they are most likely associated with noise. Given these elements, we will not consider these events to be induced by thermal or chemical stimulations.

## 3.2 Seismicity and injection history

Figure 2 shows the temporal evolution of seismicity detected during thermal and hydraulic stimulations and 4.5 days after hydraulic stimulation, the so-called post-hydraulic phase (Table 1). The time evolution of the stimulation operation parameters is also shown: injection flow rate (in l/s), wellhead pressure (WHP, in MPa) (Baujard et al., 2017; Maurer et al., 2020).

Figure 2a confirms the delayed onset of seismicity associated with thermal stimulation as previously observed by Maurer et al. (2020). However, since the seismicity detection level is lower in this study when using template matching, the triggering delay is found to be shorter, approximately 24 h after injection starts. It coincides with the third step of flow rate increase (20 l/s). The WHP was at the start of seismicity at its maximum value of 2.8 MPa for the second time (Figure 2a). There is also confirmation that seismicity stopped before shut-in, when the flow rate was still at its maximum of 25 l/s but the WHP was decreasing. A delayed occurrence of seismicity is also observed in the case of hydraulic stimulation, circa 5.5 h after the injection started (Figure 2b). In this phase, seismicity was mostly initiated at the flow rate of 40 l/s, a rate significantly higher than that of the onset of seismicity during the thermal phase (20 l/s) but at a lower WHP, 2 MPa instead of 2.8 MPa. During the hydraulic stimulation, the seismic rates are significantly larger than those calculated by Maurer et al. (2020), based on a STA/LTA detection process, and those calculated by Lengliné et al. (2017), with a maximum rate of 216 events per 30 min. This shows that the applied template matching appropriately processes sequences with high seismic rate. The seismic rate seems to increase, in average, with increasing injection flow rate and average WHP. However, this observation should be balanced by the varying magnitude of completeness, which decreases significantly during the first 7 hours of induced seismicity, i.e., during the 40 l/s and 50 l/s injection flow rates (Figure 3). Sudden increases in the seismicity rate are clearly observed when the injection flow rate also varies suddenly during the build-up phase. A clear decrease in seismicity is visible when the injection steps down from its maximum 80 l/s. Interestingly, only a few events, all smaller than −0.2 $M_{Lv}$, were observed during the second part of the injection test (from 28 June, 8:00 to 16:00) even if the flow rate has reached a level (60 l/s) higher than the one that triggered seismicity during the first part of the test (40 l/s). During this second part, the WHP is mostly below 2 MPa, the threshold above which seismicity develops during the first part of the stimulation, suggesting an improvement of injectivity during the first part. After hydraulic stimulation (on the 28th of June), no injection nor production was carried out on site. However, around 4.5 days later, on second of July, in less than 2 hours, from 04:44 to 06:38, 80% of all events detected after injection test occurred (Figure 2c). This burst of seismicity also contains the largest magnitude event recorded at the Rittershoffen site at that time, 1.55 $M_{Lv}$, substantially larger than the maximum induced during the hydraulic stimulation, 0.91 $M_{Lv}$.

As can be observed in Figure 3 (but also visible in Figures 2a,b), the minimum magnitude of the recorded events varies as a function of the time of day, being lower during the night and higher during the day. It highlights that the magnitude of completeness varies between nights and days from approximately −1.5 to −0.6 during thermal stimulation (blue squares) and between −2 and −1 during hydraulic stimulation when five seismic stations were added to the network (green circles). Interestingly, with the addition of three

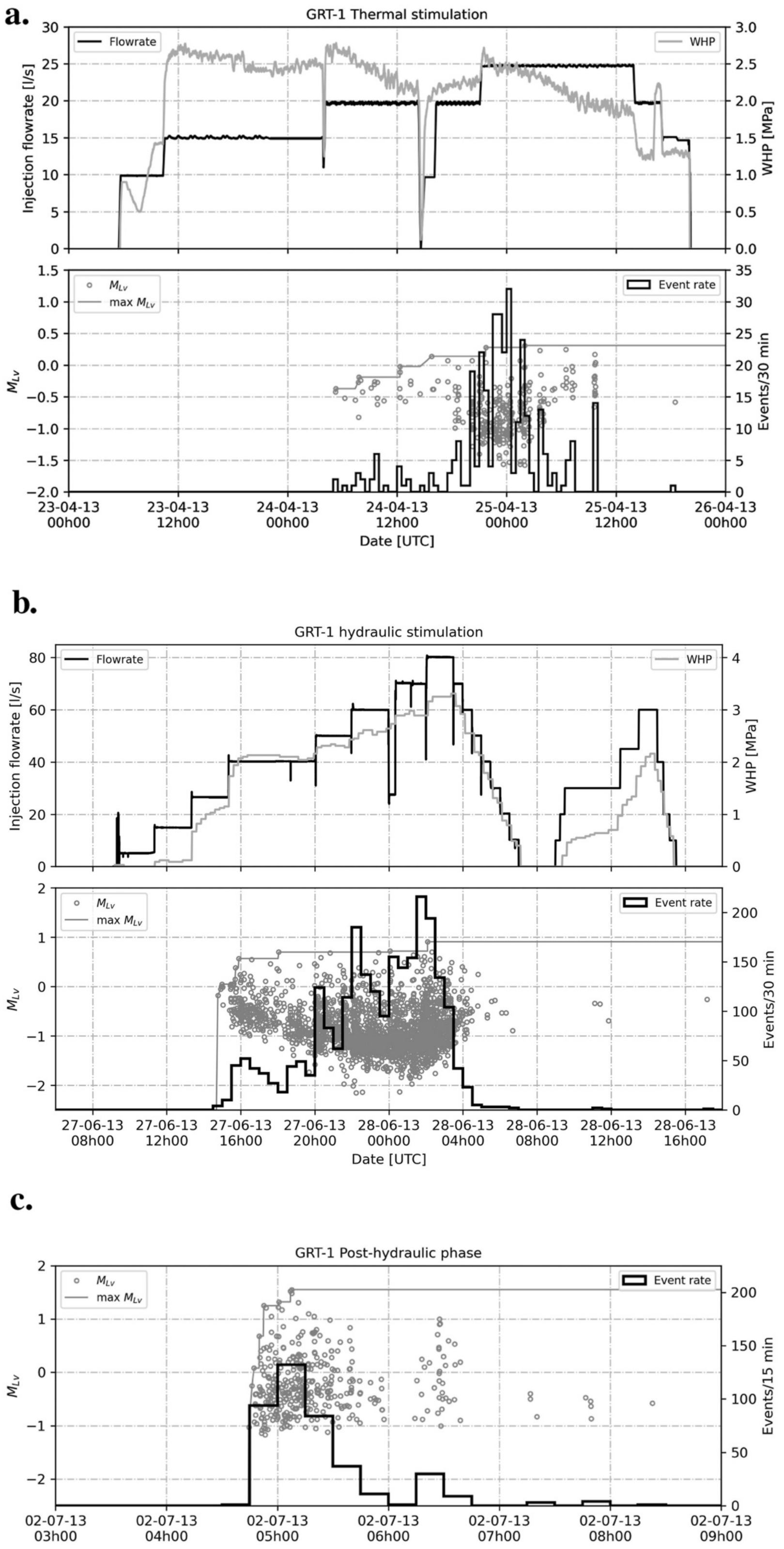

FIGURE 2
**(a)** GRT-1 thermal stimulation phase in parallel with the induced seismicity. Top: injection flowrate (l/s) (left axis, black curve) and GRT-1 wellhead pressure (MPa) (right axis, gray curve) (modified after Maurer et al. (2020)); Bottom: histogram of the number of seismic events per 30 min (right axis, black bars) and associated $M_{Lv}$ magnitudes (left axis, gray circles) with tracking of the maximum magnitude value (thin gray line). **(b)** GRT-1 hydraulic stimulation phase in parallel with the induced seismicity. Same representation as in **(a)** (modified after Maurer et al. (2020)). **(c)** Seismicity induced after GRT-1 hydraulic stimulation shut-in, defined as the post-hydraulic phase. Since there is no injection during this phase, only the number of seismic events per 15 min (right axis, black bars) and associated $M_{Lv}$ magnitudes (left axis, gray circles) with tracking of the maximum magnitude value (thin gray line) are shown.

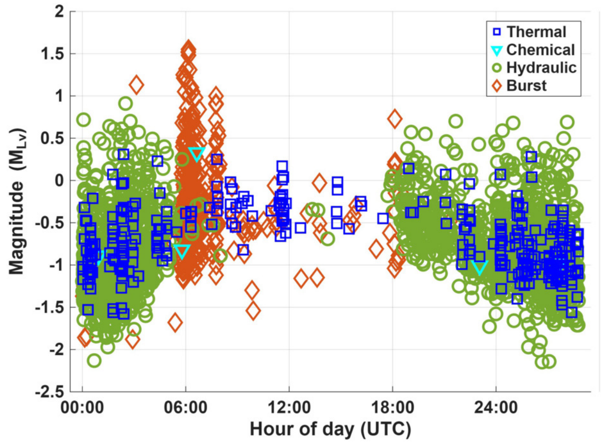

FIGURE 3
Local magnitude ($M_{LV}$) as a function of the time of the day. The four sequences with seismic events are color coded.

more stations prior to the burst of seismicity, the magnitude of completeness decreased again (orange diamonds). It should also be noted from Figure 2 that during injection, the largest magnitudes are almost constant over time and are decoupled with the injection rate and the WHP.

## 3.3 Seismicity location

Figure 4 shows the locations of the epicenters of the seismic events following the procedure introduced in Sections 2.2.1, 2.2.2. All the 3298 events are plotted; however, they are differentiated according to several quality factors. All events for which the magnitude has been determined and the relative location uncertainties are lower than or equal to the thresholds detailed below, are considered of high quality (80% of the whole dataset) and are displayed as blue points. As seen in Figure 4, these events are strongly clustered in an area of about 1000 × 250 $m^2$. The threshold values are defined on the horizontal and vertical uncertainties of the relative locations and correspond to the upper inner fence[2] values: respectively 24 m and 43 m. These thresholds are exceeded by 17% of the hypocenters, which are displayed as black circles. For all relatively located events, the median and mean of the hypocenter location uncertainties are respectively 11 m and 37 m horizontally, and 14 m and 39 m vertically. Not relatively located events, i.e., events with absolute location only, are shown in red. This concerns 1.7% of the catalog and, among them, four template events. Events for which the magnitude could not be estimated (4%) are also shown in orange.

According to these quality criteria, none of the five events that occurred during the injection test and the chemical stimulation phases (see Table 1) are of high quality.

After applying our processing workflow, the seismic events are more clustered compared to the results provided by Maurer et al. (2020). This is not only for the epicenter locations but more importantly for the hypocenter depths, reducing the large vertical spreading of the hypocenter distribution existing in their catalog. In the present catalog, all high-quality events range between 2012 m and 2700 m b.s.l., with a mean at 2256 m b.s.l. As mentioned above, the current catalog also doubles the number of events compared to those identified by Lengliné et al. (2017) and includes thermal and chemical stimulations. The main geometrical features they could identify are confirmed by our results, as discussed in Section 4.1, where more details about the spatial and time distribution of the induced seismicity are given.

# 4 Discussion

## 4.1 Seismicity distribution in space and time

### 4.1.1 High-quality seismicity analysis

Figure 5 shows the space and time distribution of induced seismic events that have been relatively located and are of high quality (see Section 3.3). The projection of the hypocenters, on a map (left-hand side) and on a north-south vertical plane (right-hand side), are color coded according to the seismogenic periods: thermal stimulation in blue (from 22/06/2013 to 27/06/2013), hydraulic stimulation in green to yellow (from 27/06/2013 to 29/06/2013) and post-hydraulic phase in red to black (after 29/06/2013). The position of the first event is emphasized by the white diamond on the GRT-1 well trajectory.

In Figure 5 it can be seen that the seismicity induced during the thermal stimulation is totally overlaid by that of the hydraulic stimulation. We observe that the first events of the hydraulic stimulation occurred in places where the thermal stimulation induced events. To confirm this overlay, we meshed the entire seismogenic volume in cubes of 30-m side, which corresponds to two to three times the median of the location uncertainties (see Section 2.2.2). We estimated the volume activated during thermal stimulation by adding the volume of the cubes that contained at least one good-quality event during thermal stimulation. Then, in this volume, we added the volume of the cubes that contained at least one good-quality event induced during hydraulic stimulation. Consequently, we obtained that 75% of the volume activated during thermal stimulation was reactivated during hydraulic stimulation.

This observation appears to contradict the common finding observed on other stimulated EGS that induced seismicity does not develop in a zone that has previously been stimulated unless the injection pressure are larger than before (e.g., Baisch et al., 2009; Caló et al., 2014; Kwiatek et al., 2014). This is the so-called Kaiser effect or “crustal memory” effect (Kaiser, 1950; Lavrov, 2003). Indeed, as observed in Figure 2b, more than half of the seismicity induced during the step-up phase of the hydraulic stimulation occurred at WHP lower than the maximum WHP observed during thermal stimulation (2.7 MPa).

Two important features of the stimulation series can be raised to explain the seismicity overlap. First, a thermal stimulation is usually intended to affect the short-range neighborhood of the wells

---

[2] The upper inner fence of a statistical sample is defined as the third quartile plus 1.5 times the inter-quartile range of this statistical sample.

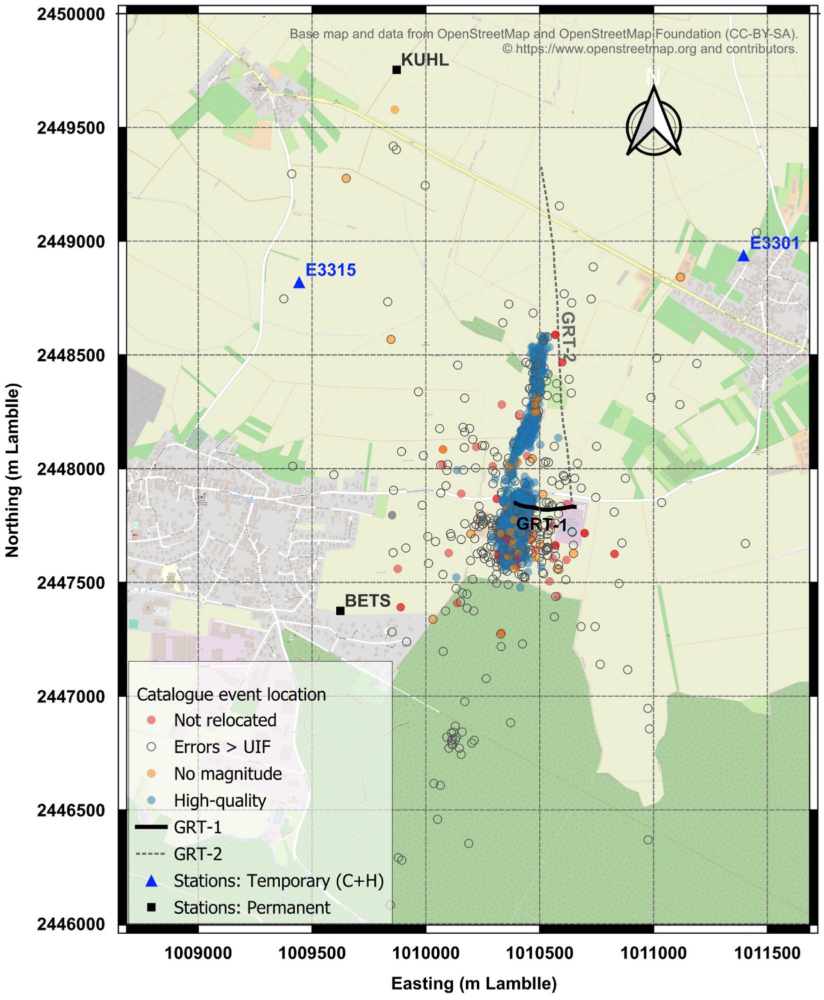

FIGURE 4
Epicenter map of the seismicity induced by the GRT-1 stimulations. Epicenters are color coded according to quality indicators: red points for non-relatively located events, black circles for events with outlying horizontal or vertical location uncertainties (i.e., larger than the upper inner fence “UIF” value), orange points for events without magnitude estimate, and, finally, blue points for events considered of high quality, that is with magnitude estimate and without outlying location uncertainties. See text for more details.

by cooling the formation with the fluid injection. However, the seismicity associated with the present thermal stimulation extends almost as far as the seismicity induced during hydraulic stimulation. It suggests that the so-called thermal stimulation had not only thermal, but also hydraulic effects. It should also be recalled that the temperature of the injected fluid was similar for both stimulations, close to 10 °C. Second, chemical stimulation took place between the thermal and hydraulic stimulations. The purpose of chemical stimulation was to increase hydraulic injectivity by chemical interaction between the injected fluid and the rock, which was likely successful, as shown by the injectivity index that increased after chemical stimulation compared to its value after thermal stimulation (see Table 1; Section 4.3.2). Therefore, chemical stimulation may have affected the thermally stimulated domain, for example, by creating new pathways close to the well and along those active during thermal stimulation. This would have had the effect of restoring the initial hydro-mechanical conditions and thus leading to similar seismicity development in space during thermal and hydraulic stimulations. This interpretation is further supported by the fact that the seismicity induced during hydraulic stimulation started at lower WHP (1.1 MPa) than that at the initiation of seismicity during thermal stimulation (above 2.5 MPa) (Figures 2a,b).

Figure 5 also highlights that the seismicity at the end of the hydraulic stimulation developed to the north, along a plane, which appears spatially disconnected from the main cloud that is centered around the well and contains the seismicity of most of the thermal and hydraulic stimulations. This late seismicity is distributed on a plane connected to that of the post-injection seismicity distribution, which further extends to the north (see the reddish colored dots in Figure 5 and later for further evidence). It is noticeable that the seismic burst during the post-hydraulic phase spontaneously developed on an approximately 400 × 500 $m^2$ surface in less than 2 hours whereas the approximately 250 × 300 × 100 $m^3$ cloud around the well was built in about 46 h during thermal and hydraulic stimulations. The evolution of the b-value, which decreases from one stimulation to another and becomes lower than 1 for post-hydraulic

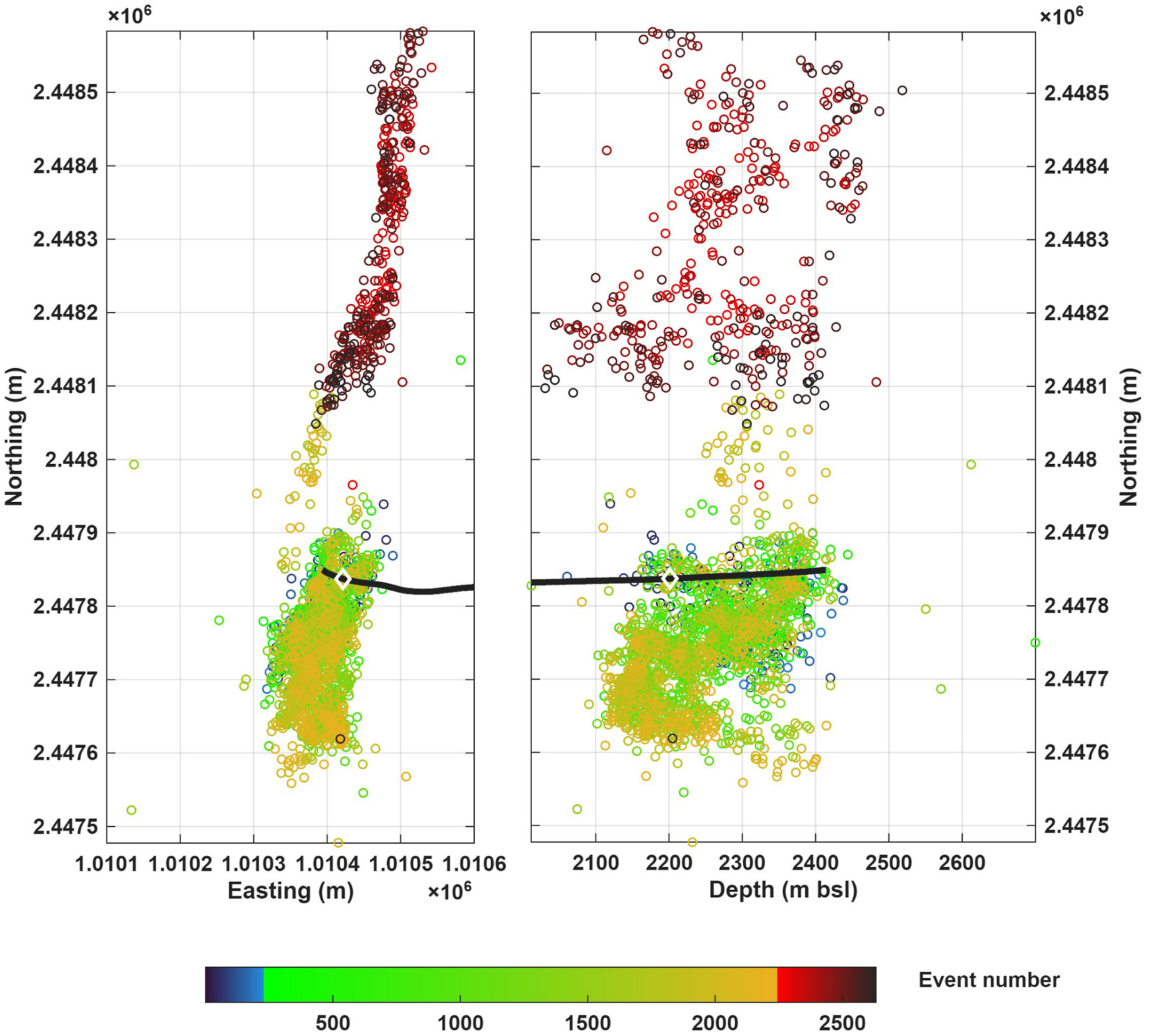

FIGURE 5
Top view (left) and side view (right) of the high-quality seismicity induced by the GRT-1 stimulations. The hypocenters are color coded according to their chronological order of occurrence. The first 228 events (blueish colors) are from the thermal stimulation. From event #229 (green to yellow colors) starts the hydraulic stimulation period and from event #2244 (red to black colors) starts the post-hydraulic injection period. The white diamond on the GRT-1 well trajectory shows the location of the first recorded event.

seismicity (see Section 4.2), is consistent with these observations, as a low b-value is the signature of natural seismicity along pre-stressed fault zones (Zang et al., 2014).

### 4.1.2 Cluster analysis

To further investigate the space and time distribution of the seismicity, spatial clustering of all seismic events was performed independently of the seismogenic period. We applied the density-based clustering approach DBSCAN proposed by Ester et al. (1996), which is implemented in the Matlab (2024) software. For reliability purposes, clustering was applied to only high-quality events.

A minimum of five hypocenters within a radius equal to the maximum between the upper inner fence of the horizontal or vertical hypocenter uncertainty, i.e., 27.5 m, was chosen to define the so-called core point. Following the clustering, the best fitting plane was computed for each cluster and its representativeness is given by the planarity value to compare with the linearity and sphericity values (Gaucher, 1998).

Figure 6 shows the time distribution of seismic events within each cluster. The first cluster, Cluster 1, is the only one that is active during all seismogenic periods, from thermal stimulation (not represented in Figure 6) to the burst of seismicity of the post-hydraulic phase (Figure 6a). Then, Cluster 2 and Cluster 3 appear when the stimulation reaches the two highest injection rates (Cluster 1 remaining active). While Cluster 2 is only activated by the hydraulic stimulation, Cluster 3 also contains the first events of the seismic burst of the post-hydraulic phase as well as the

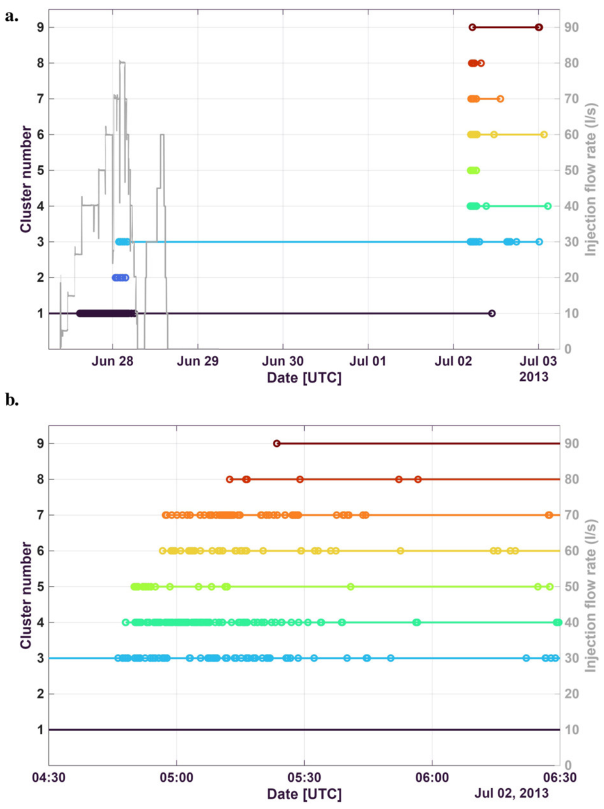

FIGURE 6
**(a)** Time occurrence of the seismic events (circles) within each cluster during the hydraulic stimulation and the post-stimulation sequences. Each cluster is represented by one specific color. The gray curve shows the fluid injection flow rate whose values (in l/s) are given by the right-hand side y-axis. **(b)** Zoom on the most seismogenic part of the post-hydraulic phase (during which no injection took place). Cluster 1 (purple color) was the only cluster active during the thermal stimulation (which is not represented here). Clusters 4 to 9 have been activated only after the hydraulic stimulation (i.e., during the post-hydraulic phase).

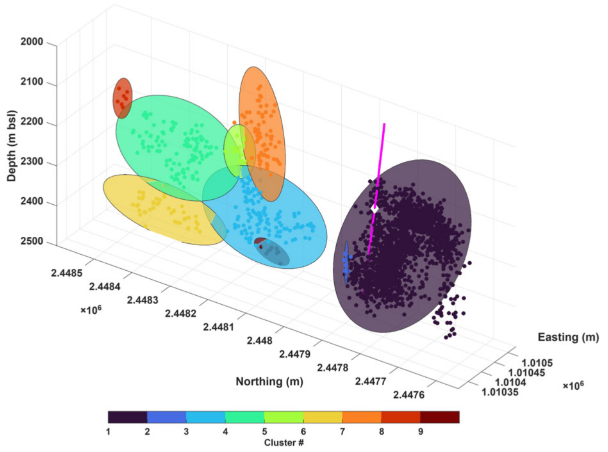

FIGURE 7
Best planes fitting the nine clusters that have been identified. The GRT-1 trajectory in this depth interval is shown in magenta and the position of the first event with the white diamond. The clusters are color coded as in Figure 6. Cluster 1 (purple color) was the only cluster active during the thermal stimulation that remained active afterwards too. Cluster 2 (dark blue) occurred only during hydraulic stimulation. Cluster 3 (light blue) was active during and after the hydraulic stimulation. Clusters 4 to 9 were active only during the post-hydraulic phase.

subsequent ones. The six following clusters (from 4 to 9) initiate one after the other and last for most of the burst sequence of the post-hydraulic phase (Figure 6b).

For each identified cluster, the cross-correlation coefficients between all pairs of events were calculated. A similar calculation was done between all pairs of non-clustered events. The results show that all clusters but Cluster 2, which contains only six events, have a median and mean cross-correlation coefficients larger than those obtained between non-clustered events. The median value of the latter equals 0.63 while the medians of the former range between 0.64 and 0.68. The smallest values are observed for Clusters 1 and 9, the largest values (0.67 and 0.68) for Clusters 7, 8 and 5. This shows that the spatial clustering is also accompanied by waveform clustering. (More details can be found in Supplementary Table S1; Supplementary Figure S2).

Figure 7 shows the seismic events colored according to the cluster they belong to, as shown in Figure 6, as well as the best fitting plane. As seen in Table 2, the first two clusters and the last one are not very well represented by planes since the planarity value is smaller than the sphericity value. This is visually clear for Cluster 1, which contains the seismicity induced by thermal stimulation and most of that from hydraulic stimulation. This also confirms the rather 3-D development of this cluster around the well during these phases. However, interestingly, the best-fit plane of this cluster, which dips 78° in a 286° direction, is fairly consistent with the orientation of the main fault as given by Vidal et al. (2016): 72°/275°. The clustering does not show any spatial continuity between the first two clusters and Cluster 3, which also contains the first events of the seismic burst (Figure 6). This may evidence a specific signature of the seismicity occurring at the end of the hydraulic stimulation. The large structure depicted by the burst of seismicity is split into seven clusters, which are reliably represented by planes (except for the last one) and which emphasize the 2-D development of this seismic sequence within few hours. Hence, several seismogenic patches are distinguished with dips varying between 77° and 90° for dip directions between N271° and N297°. Except for Clusters 4 and 5 (green and light green, respectively) and Clusters 3 and 7 (blue and orange, respectively), the plane orientations are different for each cluster. However, the northern planes have the tendency to strike in the north direction, unlike the other ones that strike more to the east. These distinct clusters may highlight different parts of the same major Rittershoffen fault zone targeted by the geothermal wells (Maurer et al., 2020).

## 4.2 b-values

Based on the newly generated catalog and the high-quality events, b-values are calculated for the three main seismogenic phases, that is, thermal stimulation, hydraulic stimulation, and post-hydraulic stimulation. To do so, four different methods have been considered and compared. They are the Aki/Wiemer-Wyss (Wiemer

TABLE 2 **Dip and dip direction of the best fitting plane for each cluster whose number of events is given. The plane representativeness is quantified by the planarity value that must be larger than the linearity and sphericity values.**

| Cluster | Dip (°) | Dip dir. (°) | Event nb | Linearity | Planarity | Sphericity |
|---|---|---|---|---|---|---|
| 1 | 78 | 286 | 2145 | 0.21 | 0.39 | 0.41 |
| 2 | 86 | 317 | 6 | 0.20 | 0.26 | 0.54 |
| 3 | 82 | 292 | 119 | 0.36 | 0.44 | 0.20 |
| 4 | 77 | 278 | 104 | 0.23 | 0.62 | 0.16 |
| 5 | 78 | 279 | 20 | 0.12 | 0.63 | 0.26 |
| 6 | 90 | 271 | 49 | 0.38 | 0.41 | 0.20 |
| 7 | 81 | 297 | 71 | 0.19 | 0.50 | 0.31 |
| 8 | 79 | 289 | 7 | 0.17 | 0.47 | 0.36 |
| 9 | 82 | 98 | 10 | 0.23 | 0.34 | 0.44 |

TABLE 3 **Comparison of b-values calculated for the three main seismogenic phases: thermal stimulation, hydraulic stimulation and post-hydraulic phase. The values estimated by Maurer et al. (2020) are recalled (first row) and several other methods have been used “Aki/Wiemer-Wyss” (Wiemer and Wyss, 2000; Aki, 1965), “b-positive” (van der Els. 2021), “b-more-positive” (Lippiello and Petrillo, 2024) and “b-more-incomplete” (Lippiello and Petrillo, 2024). Only high-quality events are consider for estimating the b-values and their number is given in parentheses.**

| Applied method | Thermal | Hydraulic | Post-hydraulic |
|---|---|---|---|
| Maurer et al. (2020) | 1.53 ± 0.15 | 1.16 ± 0.05 | 0.92 ± 0.08 |
| Aki/Wiemer-Wyss | 1.48 ± 0.12 (54) | 1.27 ± 0.05 (107) | 0.81 ± 0.05 (116) |
| b-positive | 1.45 ± 0.14 (113) | 1.08 ± 0.03 (959) | 0.80 ± 0.06 (179) |
| b-more-positive | 1.59 ± 0.11 (222) | 1.16 ± 0.03 (2007) | 0.87 ± 0.04 (381) |
| b-more-incomplete | 1.59 ± 0.11 (221) | 1.16 ± 0.03 (1962) | 0.86 ± 0.04 (373) |

and Wyss, 2000; Aki, 1965), the b-positive (van der Elst, 2021), the b-more-positive and b-more-incomplete (Lippiello and Petrillo, 2024) methods. For the last three, the minimum magnitude difference was set at 0.02, and the blind time to 2 s. Table 3 provides all the b-values computed and indicates the number of events used to calculate each of them. As a reminder, the b-values provided by Maurer et al. (2020) are also given.

For the thermal and post-hydraulic phases, the b-values provided by the four methods are consistent within the uncertainty range. However, for the hydraulic phase, the Aki/Wiemer-Wyss and b-positive methods give different results than the b-more-positive and b-more-incomplete ones. Nevertheless, for a given method, a similar trend appears: the b-value is the largest, larger than 1.44, during thermal stimulation, then decreases during hydraulic stimulation to range between 1.08 and 1.27, and decreases once more after hydraulic stimulation during the seismic burst of the post-hydraulic phase to values smaller than 0.87. Each decrease is significantly larger than the uncertainties of the b-value. So, as noticed in previous work (Maurer et al., 2020; Lengliné et al., 2017) but confirmed by our analysis, while the b-value is larger than 1 during both stimulations, it decreases significantly below 1 during the burst of seismicity of the post-hydraulic phase, which is consistent with observations from other EGS sites (Zang et al., 2014).

Since part of the volume activated during thermal stimulation was reactivated during hydraulic stimulation, Table 4 shows the b-values obtained for the events induced during hydraulic stimulation in the volume overlapping the thermal stimulation and also outside it. Again, the Aki/Wiemer-Wyss and b-positive methods give different results than the b-more-positive and b-more-incomplete ones. However, independently of the method used (despite at the limit for the Aki/Wiemer-Wyss), the b-values of the events in the overlapping volume are all smaller than the b-values of the events induced by hydraulic stimulation in the newly activated volume.

Both results suggest that stimulation in a new volume would exhibit b-values significantly larger than 1 that could be interpreted as the signature of an initial volumetric activation of small induced fractures. On the contrary, lower b-values would correspond to a shift towards reactivation of an existing fault system, natural or already created. The very significant low b-value of the delayed burst of seismicity during post-hydraulic phase can be interpreted as the triggered reactivation of a natural tectonic fault system. This interpretation is also supported by the space-time evolution of the seismicity discussed in the previous sections. The differentiated analysis of the b-value for the events induced by hydraulic stimulation in or outside the volume activated during thermal stimulation also suggests a transition from an already fractured zone to an undisturbed zone.

## 4.3 Seismicity and injection operations

Since GRT-1 stimulations in 2013, several approaches and models have been proposed to describe and follow the seismicity

TABLE 4 Comparison of b-values calculated for the events induced during the hydraulic stimulation in the volume overlapping the thermal stimulation (second column) or outside it (third column). Only high-quality events are considered for estimating the b-values and their number is given in parentheses. The four different calculation methods are used again (see Table 3).

| Applied method | Inside "thermal volume" | Outside "thermal volume" |
|---|---|---|
| Aki/Wiemer-Wyss | 1.30 ± 0.08 (67) | 1.45 ± 0.08 (84) |
| b-positive | 0.90 ± 0.05 (354) | 1.12 ± 0.05 (582) |
| b-more-positive | 1.01 ± 0.04 (760) | 1.23 ± 0.04 (1243) |
| b-more-incomplete | 1.00 ± 0.04 (748) | 1.24 ± 0.04 (1249) |

induced during stimulations as a function of operational parameters. The goal is to obtain indicators that could predict induced seismic activity, providing sufficient time to mitigate it and its impact (Kwiatek et al., 2019). Typically, the maximum magnitude of the seismic event as a function of the volume injected is considered (McGarr, 2014; van der Elst et al., 2016; Galis et al., 2017). Another approach consists in looking at the seismic energy radiated as a function of the hydraulic energy injected underground during stimulation, and the evolution of this ratio over time (Kwiatek et al., 2019; Drif et al., 2024). The specific context of the development of the GRT-1 well, with its various stimulations, raises the questions of whether the thermal, chemical, and hydraulic stimulations are providing similar responses and whether they should be considered as independent injections or not.

### 4.3.1 Maximum magnitude and injected volume

To look at the evolution of the maximum magnitude as a function of the cumulative injected volume and compare with existing models and other sites, the moment magnitude $M_W$ was used (see Section 2.2.3). Figure 8 shows this evolution for the different stimulations and compares them with different models (McGarr, 2014; van der Elst et al., 2016; Galis et al., 2017). For the "McGarr model" (McGarr, 2014) (red dash-dotted line), a friction coefficient of 0.6, a shear modulus of 10 GPa, as suggested by Drif et al. (2024), and a b-value of 1.2, which is consistent with the value observed during hydraulic stimulation (see Table 3), were applied (see Equation 12 in McGarr (2014)). For the "van der Elst model" (van der Elst et al., 2016) (purple dotted lines), the same b-value of 1.2 was applied, but values of −1 and −2 for the so-called seismogenic index Σ were chosen (see Equation 5 in van der Elst et al. (2016)). For the "Galis model" (Galis et al., 2017) (gray dashed lines), the $\gamma$ values of $10^6$ and $10^7$ are used (see Equation 3 in Galis et al. (2017)).

First, we assume that thermal stimulation and hydraulic stimulation could be treated as independent injection phases because they are separated by 2 months without any operation. The results are shown by the blue and red circles in Figure 8, respectively. Hence, one can see that the response during thermal stimulation is shifted from that to hydraulic stimulation. While injection of more than 4000 $m^3$ of fluid are necessary to induce the largest $M_W$= 1.09 event of the thermal stimulation, one-10th of such a volume is necessary to reach this magnitude during hydraulic stimulation. With the injection of 4000 $m^3$ of fluid, the hydraulic stimulation led to a significantly higher maximum magnitude of $M_W$ = 1.43 (the post-hydraulic phase is not considered here). This leads to the conclusion that the maximum magnitude versus cumulative injected volume relation observed at Rittershoffen during thermal stimulation could not have been used to anticipate the response of the system to hydraulic stimulation. After the first 400 $m^3$ of fluid have been injected, the increase in maximum magnitude drops and varies from 1.24 to 1.43 with the next 3600 $m^3$ of fluid injected. This change in slope makes it difficult to linearly approximate the evolution of the maximum magnitude with the logarithm of the cumulative injected volume.

If we consider now the hydraulic stimulation as a continuation of the thermal and chemical stimulations, as shown by the green circles in Figure 8, in first order, a reasonable degree of continuity is observed, that is, an approximately linear relationship between the maximum magnitude and the logarithm of the cumulative injected volume. Hence, a "van der Elst model" with Σ = -2 or a "Galis" model with a $\gamma$ values smaller than $10^6$ may be consistent and bound the observations, however, the "McGarr" model is inconsistent by several orders of magnitude. Therefore, if only one "van der Elst model" or "Galis model" were to be applied to GRT-1, hydraulic stimulation should not be considered independent of thermal and chemical stimulations, and the injected volumes should be cumulative. However, a closer examination suggests that different models could also bound the thermal stimulation (blue circles) and the hydraulic stimulation (green circle), with a larger slope for the hydraulic stimulation model.

The evolution of the maximum magnitude as a function of the logarithm of the cumulative injected volume is punctuated by sudden jumps of variable magnitudes with low or no concurrent volume injection. The major one is associated with the seismicity burst recorded after hydraulic stimulation, which occurred without any concurrent volume injection. These magnitude jumps are observed considering the stimulations as cumulative or independent. Moreover, from one jump to another, variable volumes have been injected. Yet, these sudden jumps may be significant in terms of seismic hazard. From a predictive perspective, the main concern would be to determine which part of the observations should be used to fit a theoretical model. Therefore, the GRT-1 stimulation case is a good example of the limitation of monitoring the maximum magnitude evolution as a function of the injected volume for hazard assessment.

### 4.3.2 Seismic energy and hydraulic energy

We follow Drif et al. (2024) to calculate the cumulative release of seismic energy and the cumulative hydraulic energy injected into the reservoir. The hydraulic energy, $E_H$, injected between times $t_i$ and $t_f$

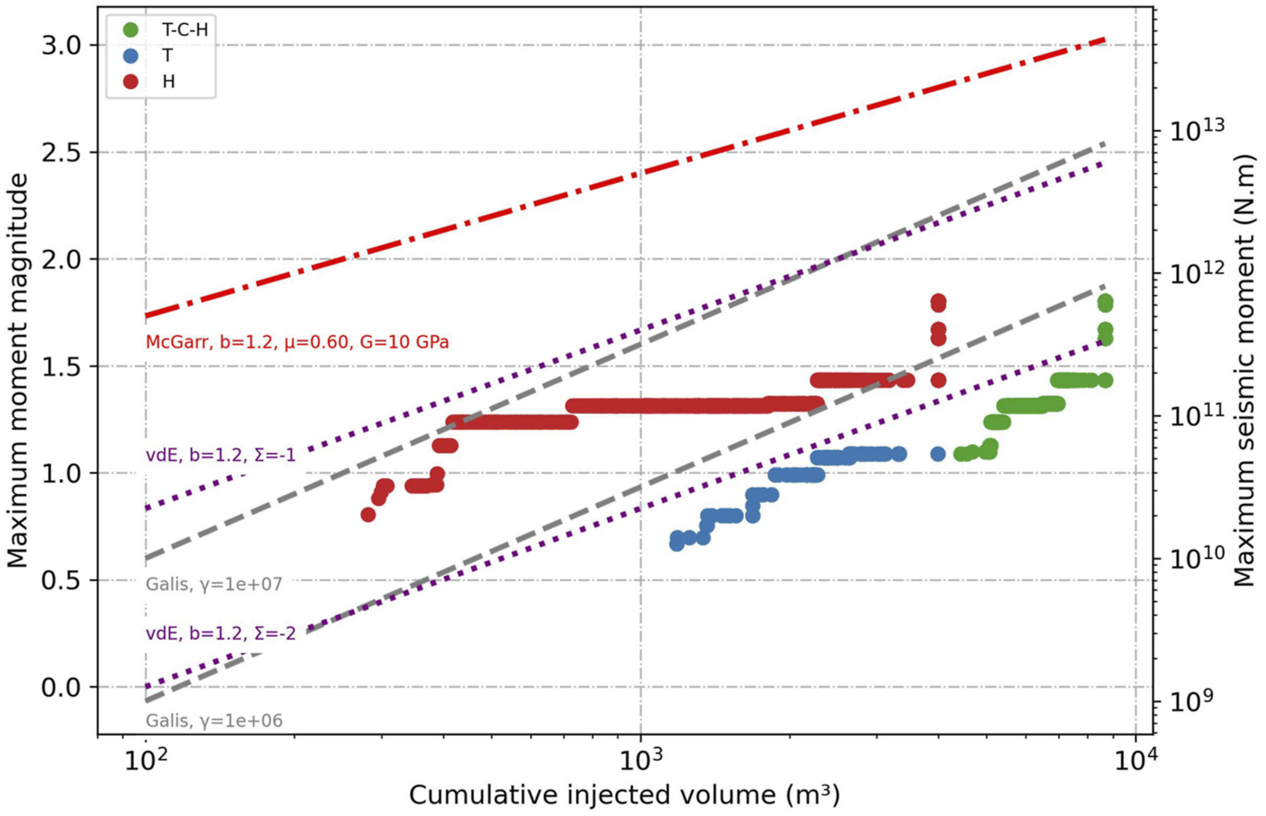

FIGURE 8
Maximum moment magnitude (left axis) or maximum seismic moment (right axis) as a function of the cumulative injected volume ($m^3$) in semi-logarithmic or log-log scales, respectively. The volume injected during the hydraulic stimulation was considered either separated (H, red dots) from the thermal (T, blue dots) and the chemical stimulations, or not (T-C-H, green dots). Reference models from McGarr (2014), van der Elst et al. (2016) and Galis et al. (2017) are shown with the associated parameters. See text for more details.

is equal to the integral of the wellhead pressure, $WHP(t)$, times the injection flow rate, $Q(t)$, as per Equation 6 in Drif et al. (2024):

$$E_H = \int_{t_i}^{t_f} WHP(t)\,Q(t)\,dt.$$

The seismic energy radiated by one seismic event is calculated according to Equation 16 in Drif et al. (2024):

$$E_R = M_0 \frac{\Delta\sigma}{2\mu}\eta_R,$$

with $\Delta\sigma$ the stress drop assumed to be 3 MPa, $\mu$ the shear modulus equal to 10 GPa as before, $\eta_R$ the radiation efficiency coefficient taken equal to 0.46 and $M_0$ the seismic moment calculated according to Hanks and Kanamori (1979) from the event moment magnitude $M_W$. All parameters, except $M_0$, are assumed to be constant across all seismic events. The seismic energy radiated between times $t_i$ and $t_f$ is the sum of the seismic energy radiated by the seismic events that occurred during this period (also written $E_R$ in the following).

Figure 9 shows the cumulative seismic energy radiated (dots on the line) and the instantaneous injectivity index (thin line) as a function of the cumulative hydraulic energy injected into the reservoir, under the assumption that thermal (T, blue), chemical (T-C, purple) and hydraulic (T-C-H, green) stimulations accumulate. To consider hydraulic stimulation independent of the other two, the green curve should simply be shifted to start at (0, 0). The instantaneous injectivity index, $III(t)$, is calculated by dividing the injection flow rate at time $t$ by the wellhead pressure measured at the same time:

$$III(t) = \frac{Q(t)}{WHP(t)}.$$

Unlike the standard injectivity index, the instantaneous injectivity index does not require the hydraulic regime to be steady state in order to be estimated.

Figure 9 highlights that the seismic energy radiated as a function of hydraulic energy during thermal stimulation (blue dots over the line) is different than during hydraulic stimulation (green dots over the line), the thermal stimulation being weakly seismogenic compared to the hydraulic stimulation. This change of behavior may partly result from the chemical stimulation. For the same amount of injected hydraulic energy, 7500 MJ, approximately 100 MJ of seismic energy is radiated during thermal stimulation against approximately 700 MJ during hydraulic stimulation. In other words, the seismic injection efficiency (e.g., Kwiatek et al., 2019; Drif et al., 2024) is different during thermal stimulation and hydraulic stimulation (slopes of the red dashed lines in Figure 9 are significantly different). Interestingly, a relatively constant slope is observed for most of

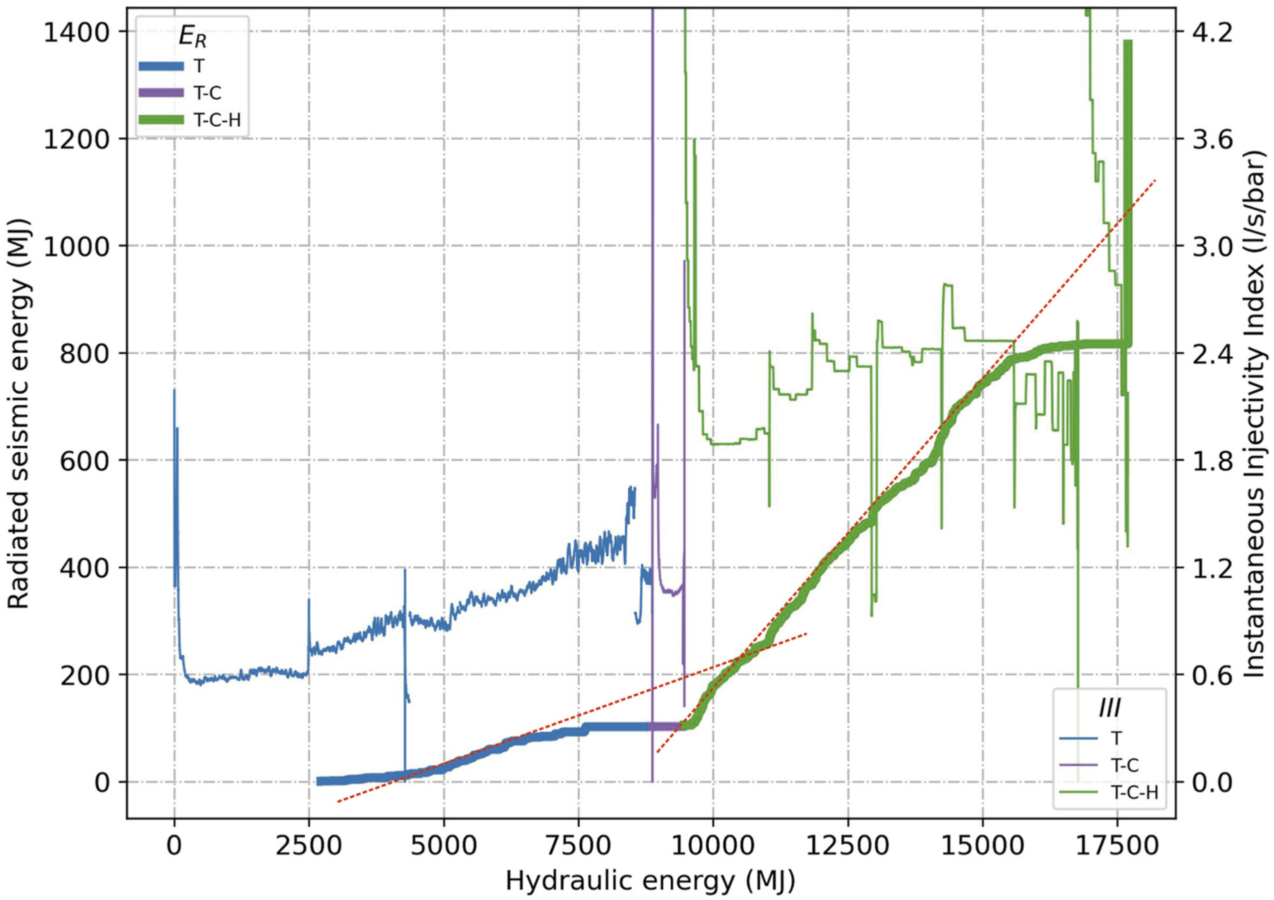

FIGURE 9
Estimated cumulative seismic energy radiated (MJ) (left axis) and instantaneous injectivity index (l/s/bar) (right axis) as a function of the cumulative hydraulic energy (MJ). The thermal ("T", in blue), chemical ("T-C", in purple) and hydraulic stimulations ("T-C-H", in green) are considered as dependent. The dashed red lines highlights the relatively constant seismic efficiency during the step-up injection phases of the thermal and hydraulic stimulations.

the hydraulic stimulation, until the step-down shut-in phase begins and a flattening occurs. This slope is approximately equal to 0.115. For thermal stimulation, the seismic efficiency varies over time. It starts very low, then increases to around 0.036 and, at the end, also flattens out. The initial low value is likely an effect of the high magnitude of completeness up to the end of the 20 l/s injection step (see Figure 2a or Figure 3) and presumably biased.

This analysis shows that the evolution of the seismic energy radiated as a function of the hydraulic energy during thermal stimulation could not have been used to anticipate the response of the system to hydraulic stimulation. However, monitoring these two parameters in relation to each other and computing the seismic efficiency, appears as a sensitive tool for deciphering each stimulation phase.

The initial constant seismic efficiency during hydraulic simulation could be interpreted as the typical seismogenic response of a reservoir with (relatively) homogeneous hydro-mechanical properties. The absence of seismicity that follows, despite continued injection, marks a different regime. This could indicate that the limit of the homogeneous reservoir has been reached. The limit may be a geostructural boundary. As seen in Section 4.1.2; Figures 6, 7, before the hydraulic stimulation shut-in begins, the seismic events start to distribute on a plane (Cluster 3) that will be active during the burst of seismicity after all injections and that is distinct from the previously active zone (Clusters 1 and 2). Hence, the transition from the 3-D distribution of events to a 2-D distribution appears to coincide with the change of the seismogenic regime. The stimulation operations would have connected the initial volumetric reservoir zone to a fault zone, as confirmed by the seismicity induced during the geothermal plant operation (Lengliné et al., 2025).

From the perspective of seismic risk assessment, it may be tempting to extend the linear trend of radiated seismic energy as a function of hydraulic energy to highlight a lack of seismic energy that will need to be compensated for at some point and possibly predict the radiated energy expected following the procedure detailed in (Drif et al., 2024). This would first implicitly assume that, in our case, the average seismogenic response of the stimulated medium does not change during the step-down shut-in phase of the thermal and hydraulic stimulations. Second, the burst of seismicity occurred 4.5 days after the hydraulic stimulation, i.e., without any injection taking place. This raises the question of "for how long" and "how" the radiated seismic energy that is apparently missing, about 250 MJ in our case, should be distributed.

From a hydraulic point of view, the series of GRT-1 stimulations have been successful since the injectivity index has increased from 0.6 l/s/bar, at the start of the thermal stimulation, to 2.5 l/s/bar, at the end of the hydraulic stimulation (according to Baujard et al. (2017)). As observed in Figure 9, the *III* increased almost linearly with the hydraulic energy injected during thermal stimulation, even during the seismic quiescence at the end of the 25 l/s flow rate (see also Figure 2a). During hydraulic stimulation, although the increase in *III* was initially proportional to the injected hydraulic energy it slowed-down from 60 l/s flow rate while the radiated seismic energy was still increasing. The radiated seismic energy quiescence occurred after the *III* flattened and the injection shut-in started. The difference in the evolution of *III* with the injected hydraulic energy (and the radiated seismic energy) may highlight that the volume stimulated during injection at a flow rate of 60 l/s does not behave as previously observed.

Monitoring the variation of the radiated seismic energy and the *III* as a function of the injected hydraulic energy looks interesting to detect changes in the behavior of the reservoir. The departure from linear evolutions could be seen as an alert for an unexpected event.

## 4.4 Stimulation versus circulation seismicity

It is of interest to compare the present analysis of the seismicity induced during the stimulation period (2013) with that of the circulation period (2016–2024) performed by Lengliné et al. (2025). The first similarity is the occurrence of bursts of seismicity rather independently of the injection conditions. Indeed, during the long term circulation, a strong intermittency of the seismicity was observed with the development of more than 80 bursts of seismicity lasting a few hours, despite a quasi-continuous injection rate. The post-hydraulic seismicity after the GRT-1 stimulation has the features of one of these bursts that occurred during the circulation period, suggesting a common triggering mechanism, such as aseismic slip. The second similarity is the spatial distribution of the seismicity. Figure 3a of Lengliné et al. (2025) shows the location of seismicity during the 2013 stimulations and that recorded during long-term circulation (2016–2024). Since the location of the seismicity recorded during the 2013 stimulations in Lengliné et al. (2025) is consistent with our (Figure 5), result comparison is possible and shows that the fault involved in the post-hydraulic stimulation is one of the existing parallel faults in the area that have been activated during circulation. Subsequently, we can conclude that the 2013 stimulations had an impact on only one of the local faults. Furthermore, one can observe that limited seismicity developed along or around the post-hydraulic seismic cloud, until 2020. This suggests that, after the 2013 stimulations, a stress memory effect was established, which only disappeared 7 years later, and that a stress shadow effect developed and prevented from further extension of the seismicity to the North (see Figure 4 of Lengliné et al. (2025)).

# 5 Conclusion

Through the application of an enhanced template matching technique and the relative location method, we have built a comprehensive catalog that covers the three stimulations that Rittershoffen GRT-1 well underwent between April and June 2013. More than 3000 seismic events are included in this catalog, which corrects the locations provided by Maurer et al. (2020) and complements the results of Lengliné et al. (2017) by including thermal and geochemical stimulations. Hence, this open-access catalog can be used as a reference for this period and for this site.

This catalog allowed us to precisely track and compare the seismogenic responses of the reservoir during the different successive stimulations (thermal, chemical, and hydraulic). In particular, it showed that the seismicity induced at the beginning of the hydraulic stimulation was located in the volume that was already active during the thermal stimulation. We interpret this as a consequence of the chemical stimulation that took place in-between and which removed the classical Kaiser effect, yet observable during the second part of the hydraulic stimulation. Interestingly, the chemical stimulation did not induce noticeable seismicity. However, the seismic sequence associated with the hydraulic stimulation further developed the volume activated during the thermal stimulation and ended with the activation of a fault segment that is reactivated during a seismic burst of the post-hydraulic phase that occurred almost 4 days after injection was terminated.

Indicators such as high to low b-value variation, sudden magnitude increase, 3-D to 2-D seismicity distribution, confined to extended spreading of the seismicity and sudden trailing-seismicity, all converge towards a seismic burst that was triggered rather than induced during the post-hydraulic stimulation phase.

The evolution of the maximum magnitude as a function of the injected volume is different between thermal and hydraulic stimulations. Similarly, the relationship between seismic energy and hydraulic energy is also different between thermal and hydraulic stimulations. This was observed when both stimulations were considered independent or part of one long and unique stimulation sequence. This may be due in part to chemical stimulation. Consequently, the responses of these indicators to the thermal stimulation of GRT-1 could not have been used to anticipate the response to the hydraulic stimulation of GRT-1, and therefore to calibrate a seismic hazard assessment model of the hydraulic stimulation from the results of the thermal stimulation.

Unlike the maximum magnitude as a function of the injected volume, the radiated seismic energy showed a smooth positive linear correlation with the injected hydraulic energy, mainly during the step-up phases of the stimulations, with evidence of departure from this linear evolution during the step-down shut-in phase or earlier. For hydraulic stimulation, this change in behavior appears at the same time as the transition from a volumetric distribution of seismicity to a distribution along a fault zone that was to be reactivated during the post-stimulation seismic burst. Furthermore, this also appears to correlate with a decline in the increase in the instantaneous injectivity index. Together, these observations indicate a change in the subsurface system response compared to the initial stable behavior, which can be seen as an alert for an unexpected event.

For seismic hazard assessment, we recommend to monitor in real-time not only the evolution of radiated seismic energy as a function of the injected hydraulic energy but also the spatial evolution of the seismicity and the instantaneous injectivity index.

## Data availability statement

The dataset presented in this study can be found in an online repository. The name of the repository and accession reference can be found below: The seismological catalog generated in this study is openly available at the CDGP (Centre de Données de Géothermie Profonde, https://cdgp.eost.unistra.fr/),a repository hosted by the University of Strasbourg, which is part of EPOS-IP Anthropogenic Hasards. The catalog belongs to the “Episode: ECOGI geothermal project at Rittershoffen - development phase” and is accessible at the following link: https://cdgp.eost.unistra.fr/geonetwork/srv/fre/catalog.search#/metadata/RITD-Catalogue-Gaucheretal.

## Author contributions

EG: Conceptualization, Data curation, Formal analysis, Investigation, Methodology, Resources, Software, Validation, Visualization, Writing – original draft, Writing – review and editing. OL: Data curation, Formal analysis, Investigation, Methodology, Resources, Software, Validation, Writing – review and editing. JS: Formal analysis, Funding acquisition, Investigation, Writing – review and editing.

## Funding

The author(s) declared that financial support was received for this work and/or its publication. This work was partly funded by the Helmholtz program “Renewable Energies” under the topic “Geothermal Energy Systems” as well as the excellence laboratory “LabEx G-EAU-THERMIE-PROFONDE” and the Interdisciplinary Thematic Institute GeoT, as part of the ITI 2021-2028-rg, CNRS and Inserm, supported by IdEx Unistra (ANR 10 IDEX 0002) and by SFRI STRAT’US project (ANR 20 SFRI 0012) (University of Strasbourg) as part of the French “Investments for the future” of the French National Research Agency.

## Acknowledgements

We thank the GEIE “Exploitation Minière de la Chaleur”, the ECOGI and ES-Géothermie companies for sharing information for this project. We are grateful to Rike Koepke and Thomas Kohl for their support and fruitful discussions, as well as to Albert Genter, Clément Baujard and Vincent Maurer for their review of an initial manuscript and fruitful discussions too. We thank Marc Schaming, Salsabyl Belalam and Benoit Derode for their support for data management. Lastly, we also thank two reviewers for their constructive comments that improved the original manuscript.

## Conflict of interest

The author(s) declared that this work was conducted in the absence of any commercial or financial relationships that could be construed as a potential conflict of interest.

## Generative AI statement

The author(s) declared that generative AI was not used in the creation of this manuscript.

Any alternative text (alt text) provided alongside figures in this article has been generated by Frontiers with the support of artificial intelligence and reasonable efforts have been made to ensure accuracy, including review by the authors wherever possible. If you identify any issues, please contact us.

## Publisher’s note

## Supplementary material

The Supplementary Material for this article can be found online at: https://www.frontiersin.org/articles/10.3389/feart.2026.1738377/full#supplementary-material

## References

Aki, K. (1965). *Maximum likelihood estimate of b in the formula logN=a-bM and its confidence limits*, 43. Bulletin of the Earthquake Research Institute, University of Tokyo, 237–239.

Axelsson, G., Thórhallsson, S., and Björnsson, G. (2006). “Stimulation of geothermal Wells in basaltic rock in Iceland,” in *ENGINE Workshop 3: stimulation of reservoir and microseismicity (Zürich, Switzerland)*.

Bagagli, M., Molinari, I., Diehl, T., Kissling, E., Giardini, D., and AlpArray Working Group (2022). The AlpArray research seismicity-catalogue. *Geophys. J. Int.* 231, 921–943. doi:10.1093/gji/ggac226

Baisch, S., Weidler, R., Voros, R., Wyborn, D., and de Graaf, L. (2006). Induced seismicity during the stimulation of a geothermal HFR reservoir in the Cooper Basin, Australia. *Bull. Seismol. Soc. Am.* 96, 2242–2256. doi:10.1785/0120050255

Baisch, S., Vörös, R., Weidler, R., and Wyborn, D. (2009). Investigation of fault mechanisms during geothermal reservoir stimulation experiments in the cooper Basin, Australia. *Bull. Seismol. Soc. Am.* 99, 148–158. doi:10.1785/0120080055

Baujard, C., Genter, A., Dalmais, E., Maurer, V., Hehn, R., Rosillette, R., et al. (2017). Hydrothermal characterization of wells GRT-1 and GRT-2 in Rittershoffen, France: implications on the understanding of natural flow systems in the rhine graben. *Geothermics* 65, 255–268. doi:10.1016/j.geothermics.2016.11.001

Bethmann, F., Deichmann, N., and Mai, P. M. (2011). Scaling relations of local magnitude *versus* moment magnitude for sequences of similar earthquakes in Switzerland. *Bull. Seismol. Soc. Am.* 101, 515–534. doi:10.1785/0120100179

Breede, K., Dzebisashvili, K., Liu, X., and Falcone, G. (2013). A systematic review of enhanced (or engineered) geothermal systems: past, present and future. *Geotherm. Energy* 1, 4. doi:10.1186/2195-9706-1-4

Caló, M., Dorbath, C., and Frogneux, M. (2014). Injection tests at the EGS reservoir of Soultz-sous-Forêts. Seismic response of the GPK4 stimulations. *Geothermics* 52, 50–58. doi:10.1016/j.geothermics.2013.10.007

Cornet, F. H., Bérard, T., and Bourouis, S. (2007). How close to failure is a granite rock mass at a 5 km depth? *Int. J. Rock Mech. Min. Sci. Geomechanics Abstr.* 44, 47–66. doi:10.1016/.j.ijrmms.2006.04.008

Cuenot, N., Dorbath, C., and Dorbath, L. (2008). Analysis of the microseismicity induced by fluid injections at the EGS site of soultz-sous-forrêts (Alsace, France): implications for the characterization of the geothermal reservoir properties. *Pure Appl. Geophys.* 165, 797–828. doi:10.1007/.s00024-008-0335-7

Danré, P., Garagash, D., De Barros, L., Cappa, F., and Ampuero, J.-P. (2024). Control of seismicity migration in earthquake swarms by injected fluid volume and aseismic crack propagation. *J. Geophys. Res. Solid Earth* 129, e2023JB027276. doi:10.1029/2023JB027276

Drif, K., Lengliné, O., Kinscher, J., and Schmitbuhl, J. (2024). Induced seismicity controlled by injected hydraulic energy: the case Study of the EGS soultz-sous-forrêts site. *J. Geophys. Res. Solid Earth* 129, e2023JB028190. doi:10.1029/2023JB028190

Ellsworth, W. L., Giardini, D., Townend, J., Ge, S., and Shimamoto, T. (2019). Triggering of the Pohang, Korea, Earthquake (Mw 5.5) by Enhanced Geothermal System Stimulation. *Seismol. Res. Lett.* 90, 1844–1858. doi:10.1785/0220190102

Ester, M., Kriegel, H.-P., Sander, J., and Xu, X. (1996). "A density-based algorithm for discovering clusters in large spatial databases with noise," in *Proceedings of the second international conference on knowledge discovery and data mining* (Portland, Oregon: AAAI Press), 226–231.

Evans, K. F., Zappone, A., Kraft, T., Deichmann, N., and Moia, F. (2012). A survey of the induced seismic responses to fluid injection in geothermal and CO2 reservoirs in Europe. *Geothermics* 41, 30–54. doi:10.1016/j.geothermics.2011.08.002

Galis, M., Ampuero, J. P., Mai, P. M., and Cappa, F. (2017). Induced seismicity provides insight into why earthquake ruptures stop. *Sci. Advances* 3, eaap7528. doi:10.1126/sciadv.aap7528

Gaucher, E. (1998). "*Comportement hydromécanique d'un massif fracturé: apport de la microsismicité induite. Application au site géothermique de Soultz-sous-Forrêts (Hydro-mechanical behaviour of a fractured rock mass: induced microseismicity contribution. Application to the Soultz-sous-Forrêts geothermal site)*," Université Paris.

Gaucher, E., Schoenball, M., Heidbach, O., Zang, A., Fokker, P. A., van Wees, J.-D., et al. (2015). Induced seismicity in geothermal reservoirs: a review of forecasting approaches. *Renew. Sustain. Energy Rev.* 52, 1473–1490. doi:10.1016/j.rser.2015.08.026

Gaucher, E., Maurer, V., and Grunberg, M. (2019). *Temporary passive seismic data acquired at Rittershoffen geothermal field Alsace, France, 2013-2014 (TOPASE)*. Potsdam, Germany: GFZ German Research Centre for Geosciences. doi:10.2312/GFZ.b103-19047

Goebel, T. H. W., and Brodsky, E. E. (2018). The spatial footprint of injection wells in a global compilation of induced earthquake sequences. *Sci. (New York, N.Y.)* 361, 899–904. doi:10.1126/science.aat5449

Grigoli, F., Cesca, S., Priolo, E., Rinaldi, A. P., Clinton, J. F., Stabile, T. A., et al. (2017). Current challenges in monitoring, discrimination, and management of induced seismicity related to underground industrial activities: a European perspective. *Rev. Geophys.* 55, 310–340. doi:10.1002/2016RG000542

Hanks, T. C., and Kanamori, H. (1979). A moment magnitude scale. *J. Geophys. Res.* 84, 2348–2350. doi:10.1029/JB084iB05p02348

Häring, M. O., Schanz, U., Ladner, F., and Dyer, B. C. (2008). Characterisation of the Basel 1 enhanced geothermal system. *Geothermics* 37, 469–495. doi:10.1016/j.geothermics.2008.06.002

Hofmann, H., Zimmermann, G., Huenges, E., Regenspurg, S., Aldaz, S., Milkereit, C., et al. (2021). Soft stimulation treatment of geothermal well RV-43 to meet the growing heat demand of Reykjavik. *Geothermics* 96, 102146. doi:10.1016/.j.geothermics.2021.102146

IEA (2024). "The future of geothermal energy," *Tech. Rep* (France: IEA Publication).

Jeanne, P., Rutqvist, J., Dobson, P. F., Walters, M., Hartline, C., and Garcia, J. (2014). The impacts of mechanical stress transfers caused by hydromechanical and thermal processes on fault stability during hydraulic stimulation in a deep geothermal reservoir. *Int. J. Rock Mech. Min. Sci.* 72, 149–163. doi:10.1016/j.ijrmms.2014.09.005

Kaiser, J. (1950). *An investigation in the occurrence of noises in tensile tests or a study of acoustic phenomena in tensile tests*. Tech. Hoch. München, Germany.

Kraft, T., and Deichmann, N. (2014). High-precision relocation and focal mechanism of the injection-induced seismicity at the Basel EGS. *Geothermics* 52, 59–73. doi:10.1016/j.geothermics.2014.05.014

Kwiatek, G., Bulut, F., Bohnhoff, M., and Dresen, G. (2014). High-resolution analysis of seismicity induced at Berlín geothermal field, El Salvador. *Geothermics* 52, 98–111. doi:10.1016/j.geothermics.2013.09.008

Kwiatek, G., Martínez-Garzón, P., Dresen, G., Bohnhoff, M., Sone, H., and Hartline, C. (2015). Effects of long-term fluid injection on induced seismicity parameters and maximum magnitude in northwestern part of the Geysers geothermal field. *J. Geophys. Res. Solid Earth* 120, 7085–7101. doi:10.1002/2015JB012362

Kwiatek, G., Saarno, T., Ader, T., Bluemle, F., Bohnhoff, M., Chendorain, M., et al. (2019). Controlling fluid-induced seismicity during a 6.1-km-deep geothermal stimulation in Finland. *Sci. Advances* 5, eaav7224. doi:10.1126/sciadv.aav7224

Lavrov, A. (2003). The Kaiser effect in rocks: principles and stress estimation techniques. *Int. J. Rock Mech. Min. Sci.* 40, 151–171. doi:10.1016/.S1365-1609(02)00138-7

Lengliné, O. (2022). DETX.

Lengliné, O., Boubacar, M., and Schmittbuhl, J. (2017). Seismicity related to the hydraulic stimulation of GRT1, Rittershoffen, France. *Geophys. J. Int.* 208, 1704–1715. doi:10.1093/gji/ggw490

Lengliné, O., Schmittbuhl, J., Drif, K., Lambotte, S., Grunberg, M., Kinscher, J., et al. (2023). The largest induced earthquakes during the GEOVEN deep geothermal project, Strasbourg, 2018-2022: from source parameters to intensity maps. *Geophys. J. Int.* 234, 2446–2458. doi:10.1093/gji/ggad255

Lengliné, O., Maurer, V., and Yorillo, A. (2025). Intermittent induced seismicity during the multiyear operation of a geothermal reservoir. *Geophys. J. Int.* 242, ggaf160. doi:10.1093/gji/ggaf160

Li, S., Wang, S., and Tang, H. (2022). Stimulation mechanism and design of enhanced geothermal systems: a comprehensive review. *Renew. Sustain. Energy Rev.* 155, 111914. doi:10.1016/j.rser.2021.111914

Lippiello, E., and Petrillo, G. (2024). b-More-Incomplete and b-More-Positive: insights on a robust estimator of magnitude distribution. *J. Geophys. Res. Solid Earth* 129, e2023JB027849. doi:10.1029/2023JB027849

Lomax, A. (2023). NonLinLoc. Original-date: 2016-04-06T08:35:08Z.

Lomax, A., Virieux, J., Volant, P., and Berge-Thierry, C. (2000). "Probabilistic earthquake location in 3D and layered models," in *Advances in seismic event location. 18 of modern approaches in geophysics*. Editors C. Thurber, and N. Rabinowitz (Springer Netherlands), 101–134. doi:10.1007/978-94-015-9536-0

Lomax, A., Michelini, A., and Curtis, A. (2009). "Earthquake location, direct, global-search methods," in *Encyclopedia of complexity and systems science*. Editor R. A. Meyers (New York: Springer), 2449–2473. doi:10.1007/978-0-387-30440-3

Majer, E. L., Baria, R., Stark, M., Oates, S., Bommer, J., Smith, B., et al. (2007). Induced seismicity associated with Enhanced Geothermal Systems. *Geothermics* 36, 185–222. doi:10.1016/j.geothermics.2007.03.003

Matlab (2024). Statistics and machine learning Toolbox (R2024a).

Maurer, V., Cuenot, N., Gaucher, E., Grunberg, M., Vergne, J., Wodling, H., et al. (2015). "Seismic monitoring of the Rittershoffen EGS project (Alsace, France)," in *World Geothermal Congress 2015 (IGA)*.

Maurer, V., Gaucher, E., Grunberg, M., Koepke, R., Pestourie, R., and Cuenot, N. (2020). Seismicity induced during the development of the Rittershoffen geothermal field, France. *Geotherm. Energy* 8, 132. doi:10.1186/.s40517-020-0155-2

McGarr, A. (2014). Maximum magnitude earthquakes induced by fluid injection. *J. Geophys. Res. Solid Earth* 119, 1008–1019. doi:10.1002/2013JB010597

McLennan, J., England, K., Rose, P., Moore, J., and Barker, B. (2023). Stimulation of a high-temperature granitic reservoir at the Utah FORGE site," in *SPE Hydraulic Fracturing Technology Conference and Exhibition*. doi:10.2118/212346-MS

Norbeck, J. H., McClure, M. W., and Horne, R. N. (2018). Field observations at the Fenton Hill enhanced geothermal system test site support mixed-mechanism stimulation. *Geothermics* 74, 135–149. doi:10.1016/j.geothermics.2018.03.003

Portier, S., Vuataz, F.-D., Nami, P., Sanjuan, B., and Gérard, A. (2009). Chemical stimulation techniques for geothermal wells: experiments on the three-well EGS system at Soultz-sous-Forrêts, France. *Geothermics* 38, 349–359. doi:10.1016/j.geothermics.2009.07.001

Ross, Z. E., Trugman, D. T., Hauksson, E., and Shearer, P. M. (2019). Searching for hidden earthquakes in Southern California. *Science* 364, 767–771. doi:10.1126/.science.aaw6888

Schmittbuhl, J., Lengline, O., Cornet, F., Cuenot, N., and Genter, A. (2014). Induced seismicity in EGS reservoir: the creep route. *Geotherm. Energy* 2, 14. doi:10.1186/.s40517-014-0014-0

Schmittbuhl, J., Lambotte, S., Lengliné, O., Grunberg, M., Jund, H., Vergne, J., et al. (2021). Induced and triggered seismicity below the city of Strasbourg, France from November 2019 to January 2021. *Comptes Rendus. Géoscience* 353, 1–24. doi:10.5802/crgeos.71

Slinkard, M., Schaff, D., Mikhailova, N., Heck, S., Young, C., and Richards, P. G. (2014). Multistation validation of waveform correlation techniques as applied to broad regional monitoring. *Bull. Seismol. Soc. Am.* 104, 2768–2781. doi:10.1785/0120140140

Slinkard, M., Heck, S., Schaff, D., Bonal, N., Daily, D., Young, C., et al. (2016). Detection of the Wenchuan Aftershock sequence using waveform correlation with a composite regional network. *Bull. Seismol. Soc. Am.* 106, 1371–1379. doi:10.1785/0120150333

Trugman, D. (2023a). GrowClust.

Trugman, D. (2023b). GrowClust3D.jl. Original-date: 2022-01-10T16:52:43Z

Trugman, D. T., Chamberlain, C. J., Savvaidis, A., and Lomax, A. (2022). GrowClust3D.jl: a julia package for the relative relocation of earthquake hypocenters using 3D velocity models. *Seismol. Res. Lett.* 94, 443–456. doi:10.1785/0220220193

van der Elst, N. J. (2021). B-Positive: a robust estimator of aftershock magnitude distribution in transiently incomplete catalogs. *J. Geophys. Res. Solid Earth* 126, e2020JB021027. doi:10.1029/2020JB021027

van der Elst, N. J., Page, M. T., Weiser, D. A., Goebel, T. H., and Hosseini, S. M. (2016). Induced earthquake magnitudes are as large as (statistically) expected. *J. Geophys. Res. Solid Earth* 121, 4575–4590. doi:10.1002/2016JB012818

Vidal, J., and Genter, A. (2018). Overview of naturally permeable fractured reservoirs in the central and southern Upper Rhine Graben: insights from geothermal wells. *Geothermics* 74, 57–73. doi:10.1016/j.geothermics.2018.02.003

Vidal, J., Genter, A., and Schmittbuhl, J. (2016). Pre- and post-stimulation characterization of geothermal well GRT-1, Rittershoffen, France: insights from acoustic image logs of hard fractured rock. *Geophys. J. Int.* 206, 845–860. doi:10.1093/gji/ggw181

Vidal, J., Genter, A., and Chopin, F. (2017). Permeable fracture zones in the hard rocks of the geothermal reservoir at Rittershoffen, France. *J. Geophys. Res. Solid Earth* 122, 4864–4887. doi:10.1002/2017JB014331

Wiemer, S., and Wyss, M. (2000). Minimum magnitude of completeness in earthquake catalogs: examples from Alaska, the Western United States, and Japan. *Bull. Seismol. Soc. Am.* 90, 859–869. doi:10.1785/.0119990114

Zang, A., Oye, V., Jousset, P., Deichmann, N., Gritto, R., McGarr, A., et al. (2014). Analysis of induced seismicity in geothermal reservoirs - an overview. *Geothermics* 52, 6–21. doi:10.1016/j.geothermics.2014.06.005